

SUPPORTING INFORMATION (SI)

***In situ* grown organo-lead bromide perovskite induced electroactive γ -phase in aerogel PVDF film: an efficient photoactive material for piezoelectric energy harvesting and photodetector application**

*Suman Kumar Si, Sarbaranjan Paria, Sumanta Kumar Karan, Suparna Ojha, Amit Kumar Das, Anirban Maitra, Aswini Bera, Lopamudra Halder, Anurima De and Bhanu Bhusan Khatua**

Materials Science Centre, Indian Institute of Technology, Kharagpur - 721302, India

*Corresponding Author: Prof. B. B. Khatua

Materials Science Centre

Indian Institute of Technology Kharagpur, Kharagpur-721302, India

Email: khatuabb@matsc.iitkgp.ernet.in

Tel: +91-3222-283982

S1: Materials

Poly-vinylidene fluoride (PVDF, Alfa-Aesar, India), polydimethylsiloxane (PDMS, Dow Corning Sylgard 184, Dow Corning Corp), lead (II) bromide, (PbBr_2 , 99.8%, Sigma Aldrich), formamidinium bromide (FABr, Dyesol, Australia), *N, N*-dimethylformamide (DMF, anhydrous, 99.8%, Merck Chemicals, India), dimethyl sulfoxide (anhydrous, 99.9%, Sigma Aldrich), commercial ITO/PET film ($5.5 \text{ cm} \times 5 \text{ cm}$, resistivity of $100 \text{ } \Omega \cdot \text{m}$, Sigma-Aldrich), were procured and used without any additional treatment or modification. Commercially available Cu foil was purchased from India.

S2: Characterization and measurements

The morphology and microstructures of porous FPNC aerogel films were characterized by the field-emission scanning electron microscopy (FESEM, Carl Zeiss-SUPRA40) and high-resolution transmission electron microscopy (HR-TEM, JEM-2100, JEOL, and Japan). The formation of FAPbBr_3 NPs in the PVDF matrix and development of the different polymorphs of PVDF in the FPNC films have been investigated using an X-ray diffractometer (XRD, Panalytical, Netherland), and Fourier transform infrared spectrophotometer (FTIR, NEXUS- 870). The optical properties of the synthesized FPNC films were studied using UV–visible spectrophotometer (Lambda 25, Perkin Elmer, USA, and UV –3101PC, Shimadzu) and Cary Eclipse fluorescence spectrophotometer (Agilent Technologies). The thermal behavior of the FPNC films has been studied by differential scanning calorimeter (DSC, Perkin Elmer Pyris). The dielectric constant of FPNC films was measured by a computer-controlled precision impedance analyzer (HIOKI 3532-50 LCR HiTESTER) through recording the capacitance (C) and tangent loss ($\tan\delta$) under the application of alternating electric field. The ferroelectric properties of the pure PVDF and FPNC films were studied by Hysteresis version 4.9.4 (Radiant Technologies) at room temperature and frequency of 100 Hz. The mechanical properties of the FPNC films with

thickness 100 μm were measured using Universal Testing Machine (Tinius Olsen model: H50KS, UK). The piezoelectric output voltage and short circuit current of the FPNG device were measured by a digital oscilloscope (ROHDE & SCHWARZ, RTM 2022, 1 M Ω) and an electrometer (Keithley 4200-SCS), respectively.

S3: EDAX spectra of FPNC (8) films

Energy dispersive X-ray analysis (EDAX) of FPNC nanocomposite film clearly revealed the presence of C, F, N, Pb, and Br in the porous FPNC films, as shown in Fig. S1.

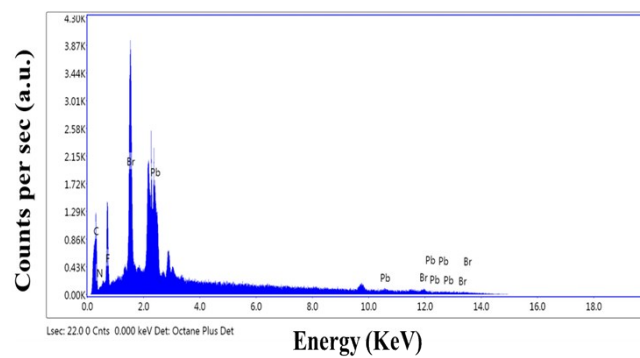


Fig. S1 EDAX spectra of porous FPNC (8) film

S4: Elemental mapping of porous FPNC films

The elemental mapping analysis of the corresponding FESEM image of FPNC film confirms the presence and the distribution of the component elements in the FPNC film, as shown in Fig. S2.

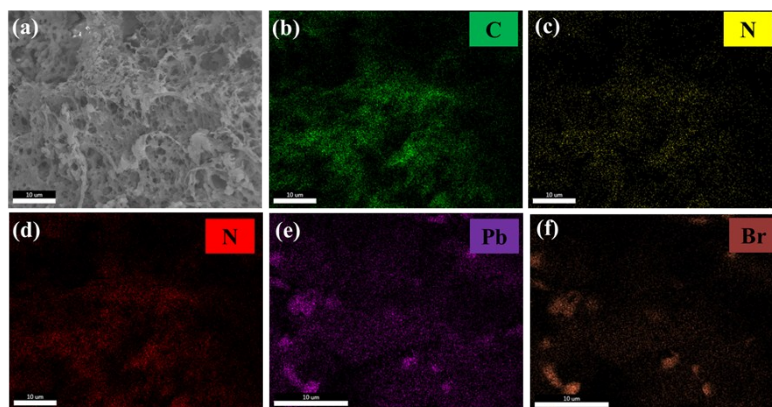


Fig. S2 (a) FESEM image of porous FPNC (8) film and corresponding elemental mapping images of (a) C, (b) N, (c) F, (d) Pb and (e) Br.

S5: Calculation of crystallinity

The degree of crystallinity (χ_c) of PVDF and FPNC films (with different wt% FAPbBr₃) was calculated using the following equation for qualitative illustration of crystallinity of PVDF and its composites:

$$\chi_c = \frac{\sum A_{cr}}{\sum A_{cr} + \sum A_{amr}} \times 100\% \quad \dots\dots\dots(\text{ES1})$$

Where, $\sum A_{cr}$ and $\sum A_{amr}$ are the summation of the integral area of the crystalline zone and amorphous zone, respectively.¹ From the calculated data, an increment in the degree of crystallinity of PVDF is evident with increasing FAPbBr₃ NPs loadings in FPNC films (as shown in Fig. S3 (b)). For PVDF, the degree of crystallinity (χ_c) is lowest (36%) but it reaches maximum (60%) with the 8 wt% of FAPbBr₃ NPs loading. Furthermore, on the further loading of FAPbBr₃ NPs, the total crystallinity of the FPNC film decreases which confirm that FPNC (8) gives the highest % of the γ -phase as well as reduction of the non-polar α -phase. The increase in the crystallinity of FPNC film in the presence of FAPbBr₃ NPs is due to the heterogeneous nucleation, which enhances the crystallization temperature by its large surface area for adsorption of the PVDF chains.^{1, 2}

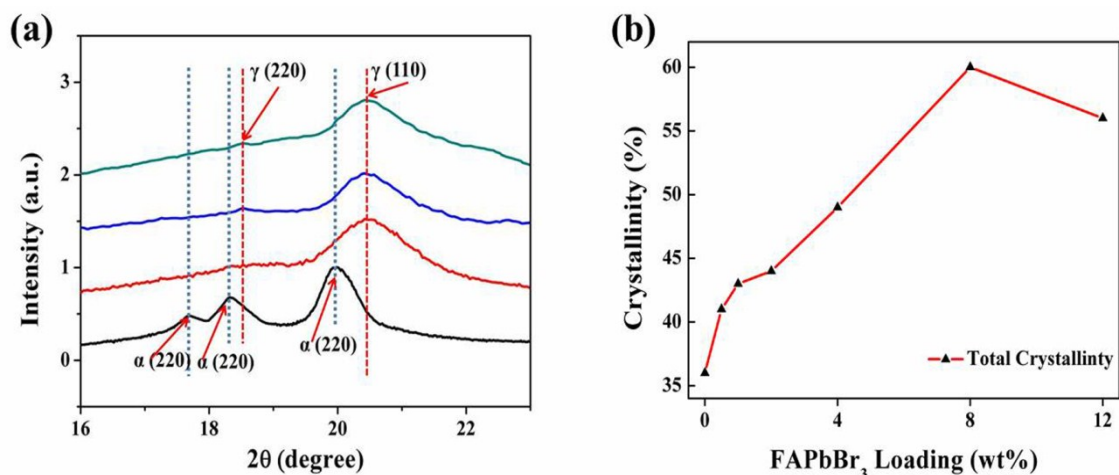


Fig. S3 (a) XRD pattern for pure PVDF and FPNC nanocomposite films in the range of 15° to 23°, (b) the variation of total crystallinity of PVDF films with the FAPbBr₃ NPs loadings in porous FPNC films.

S6: Calculation of relative proportion of electroactive polar phases

The relative percentages [F (γ)] of γ phase in the FPNC films were calculated using the following equation:

$$F(\gamma) = \frac{X_\gamma}{X_\alpha + X_\gamma} = \frac{A_\gamma}{A_\gamma + A_\alpha (K_\gamma / K_\alpha)} \dots\dots\dots (ES2)$$

Where, X_α and X_γ are the corresponding crystallinity of α and γ -phases, respectively. A_γ and A_α are the absorbances at 833, and 761 cm^{-1} , respectively and K_γ (0.365 μm^{-1}) and K_α (0.150 μm^{-1}) are absorption coefficient at the respective wave number ³. As shown in Fig. S4(b), the maximum percentage of the γ -phase is reached up to 97 % at 8 wt% FAPbBr₃ NPs loading in the PVDF matrix, but on further filler loading, the film became rough and crease which hinders further nucleation of γ -phase of PVDF in the FPNC film ². Moreover, the FTIR spectra of the FPNC (8) film in the region of 2900-3100 cm^{-1} has been provided in Fig. S4 (a) to understand the electroactive phase formations via interfacial interaction of the $-\text{CH}_2$ dipoles of PVDF chains with FAPbBr₃ NPs in the porous film. The two fundamental vibrational bands for symmetric stretching ($-\text{CH}_2$) and asymmetric stretching ($-\text{CH}_2$) of FPNC (8) films are shifted towards lower frequency as compared to pure PVDF film, as shown in the Fig. S4 (a), manifesting the interfacial interaction between FAPbBr₃ NPs and PVDF chains.^{2,3} A comparison table of electroactive phase content of insitu-FAPbBr₃ NPs incorporated PVDF porous nanocomposite film with other reported PVDF films has provided in Table S1.

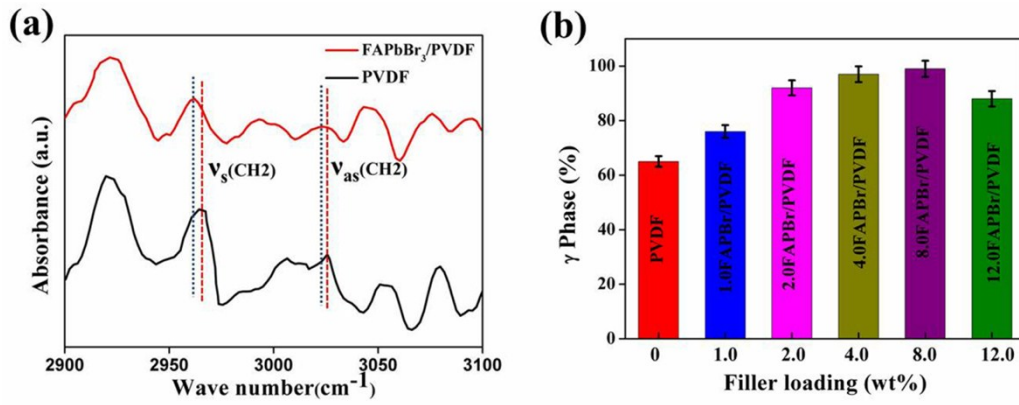


Fig. S4 (a) FT-IR spectra of pure PVDF and FPNC films in the range of 2900-3100 cm⁻¹ **(b)** the relative proportion of γ -phase (%) formation in PVDF and FPNC films.

By using the above equation, the percentage of γ -phase ($F(\gamma)$) for pure PVDF is 65% and for the FPNC (8) nanocomposite films, $F(\gamma)$ is 97 %.

Table S1: Comparison of electroactive phase content of insitu-FAPbBr₃ NPs incorporated PVDF porous nanocomposite film with other reported PVDF films.

Filler	Electroactive Phase (%)	Ref
ZnO	87	4
BaTiO ₃	80	5
CoFe ₂ O ₄	90	6
Fe-RGO	99	3
CH ₃ NH ₃ PbBr ₃	91	7
CH ₃ NH ₃ PbI ₃	91	8
CH ₃ NH ₃ PbI ₃	95	9
Insitu FAPbBr₃ NPs	97	My work

S7: Calculation of enthalpy and percentage of crystallinity (χ_c) of porous FPNC films from DSC thermographs

The calculated heat of enthalpy and crystallinity of the pure PVDF and FPNC films are presented in Fig. S5 and Table S2. The value of melting enthalpy (ΔH_m) and percentage of crystallinity (X_c) are both increased with increasing FAPbBr₃ NPs loading in the PVDF matrix. The percentage of crystallinity (χ_c) of the pure PVDF and its composites were calculated by using the equation:

$$\chi_c(\%) = \frac{\Delta H_m}{(1-\Phi)H_m^0} \times 100 \dots\dots\dots (ES3)$$

Where ΔH_m is the melting enthalpy of the nanocomposite films, ΔH_m^0 is the melting enthalpy of the 100% crystalline PVDF (104.50 J.g⁻¹), and Φ is the weight percentage of the FAPbBr₃ NPs in the nanocomposite films.^{10, 11}

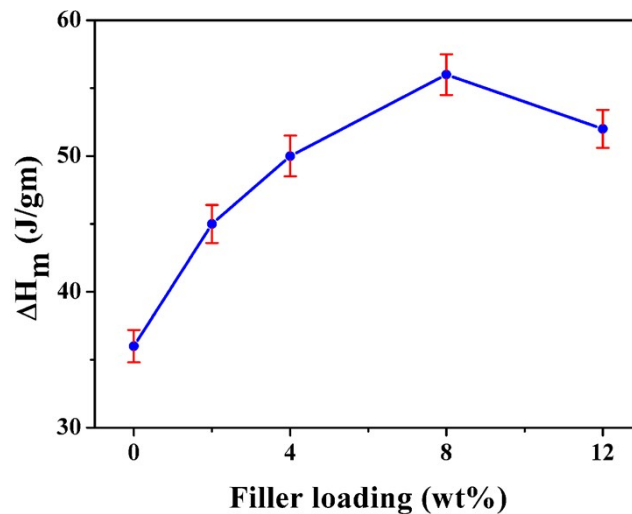


Fig. S5 Illustrates the variation of melting enthalpy of the FPNC films with FAPbBr₃ NPs content.

Table S2. Illustration of DSC parameters and χ_c values of pure PVDF and FPNC nanocomposite films at various FAPbBr₃ NPs loadings

Filler loading (%)	T _m (°C)	T _c (°C)	ΔH_m (J/g)	χ_c (%)
0.0	160.76	129.61	36.46	34.8
2.0	161.47	131.43	45.20	44.0
4.0	162.08	132.82	50.72	50.2
8.0	163.26	133.96	56.83	61.1
12.0	163.05	133.26	52.20	56.2

S8: UV–Vis absorption spectra of porous FPNC (8) film

The UV–Vis absorption spectra of FPNC (8) Films shows a broad absorption ranging from 400 to 800 nm. The band gap of FPNC film is calculated from the intercept by extrapolating the liner portion of the Tauc plot. The band gap is found to be 2.2 eV which is good agreement with previous results.

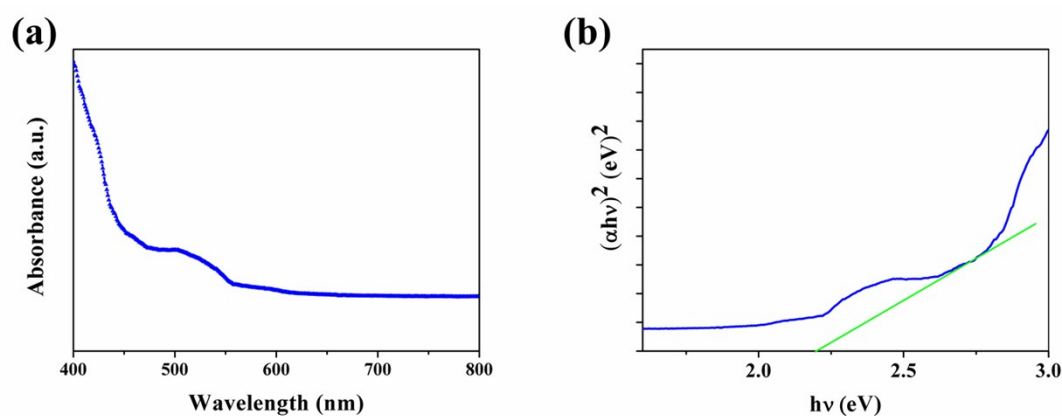


Fig. S6 (a) UV–Vis absorption spectra of porous FPNC (8) film, (b) Tauc plot for determination of the band gap energy of FPNC film.

S9: Calculation of applied pressure

Based on physical model combining the gravity term and pulse term, we have calculated the imparting pressure generated by human fingers or moving object on the FPNG. There are two steps involved in the process of falling of object on the FPNG device. Firstly, the falling object touches the surface of the device. Secondly, the falling object completely acts the pressure on the device. In case of the first process the descending velocity of the moving object reaches to the maximum value and, in case of the second process, it reaches to zero value. So, we have the following relations based on the kinetic energy theorem and momentum theorem:

$$m.g.h = \frac{1}{2}mv^2 \quad \dots\dots\dots (ES4)$$

$$(F - m.g)\Delta t = m.v \quad \dots\dots\dots (ES5)$$

$$\sigma = \frac{F}{S} \quad \dots\dots\dots (ES6)$$

Where m is the mass of the object, h is the height from where it is fall, v is the maximum falling velocity, σ is the applied pressure or applied stress, F is the applied force, S is the active contact area of device, and Δt is the period during the second process.

Here, $S = 300 \text{ mm}^2$ is the active area (effective area) of the electrode (area under the external pressure), $m = 1.51 \text{ kg}$ is measured using laboratory balance, $\Delta t = 0.22 \text{ sec}$ is the estimated average time difference between the two consecutive voltage peak, $h = 0.08 \text{ m}$ is the height and $g = 9.80 \text{ N/kg}$. Therefore, from these values, the calculated input force is $F \approx 23.4 \text{ N}$, which gives the contact pressure in the order of $\sigma \approx 78.0 \text{ kPa}$.

S10: Piezoelectric coefficient (d_{33}) measurement and calculation:

The most important parameter for piezoelectric application is the piezoelectric coefficient of samples (d_{33}). We have measured the piezoelectric coefficient (d_{33}) value of FPNC (8) nanocomposite film using a d_{33} meter (Piezotest, PM300) at 50 Hz under constant

force 0.5 N. The measured piezoelectric coefficient value of FPNC (8) nanocomposite film varies from ~ 30-32 pC/N. This inconstancy could be related to the variation of moisture absorption in the films, thickness of FPNC films and the humid condition during the measurement, as reported earlier with other piezoelectric material¹².

Using the following equation, we can also calculate the piezoelectric constant (d_{33}) theoretically,

$$d_{33} = \frac{V.C}{F} \dots\dots\dots (ES7)$$

Where, V is the output voltage, C is capacitance of the sample, and F is the imparting force. Using the value of the output voltage ($V = 26.2$ V), the capacitance value $C = 28.8$ pF at 50 Hz and the force $F = 23.4$ N, we have found d_{33} value to be 32.3 pC/N. Thus the output voltage generated by our FPNG is well consistent with the piezoelectric coefficient of our sample FPNC (8).

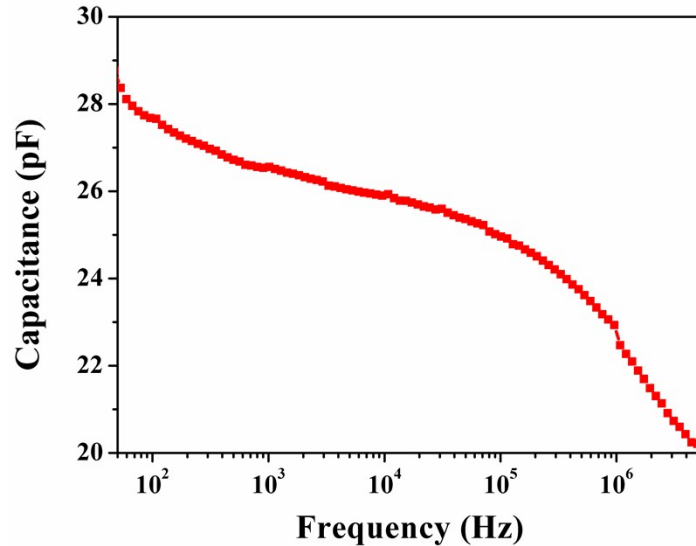


Fig. S7 The frequency dependent capacitance value of FPNC (8) sample measured using digital LCR meter (Agilent, E4980A).

Table S3: Tabulated presentation of d_{33} and output characteristics of all samples.

Sample Name	Piezoelectric Coefficient (d_{33}) (pC/N)	Output Voltage (V)	Current (μ A)
PVDF	5.5	5.2	0.41
FPNC (2)	18.5	14.8	0.89
FPNC (4)	25.2	20.3	1.64
FPNC (8)	32.3	26.2	2.1
FPNC (12)	28.2	20.5	1.7

In addition, the piezoelectric coefficient (d_{33}) can be also defined as the change in polarization under applied uniaxial stress. Also, d_{33} can be formulated as,

$$d_{33} = -\frac{P_r}{Y} \dots\dots\dots(\text{ES8})$$

Where Y is the Young's modulus, and P_r is remanent polarization is of sample. Using the above equation, the d_{33} for FPNC (8) film was calculated to be – 33.6 pC/N. In contrast, pure PVDF aerogel film has d_{33} values of -5.6 pC/N.

Table S4: Calculation of piezoelectric coefficients from young modulus data

Materials	P_r (μ C/cm ²)	Y (N/mm ²)	d_{33} (pC/N) $d_{33} = -P_r/Y$
PVDF	0.07	123	5.6
FPNC (2)	0.25	198	13
FPNC (4)	0.70	268	26.1
FPNC (8)	1.09	314	33.6

S11: The variation of Young's modulus and tensile strength of porous FPNC films

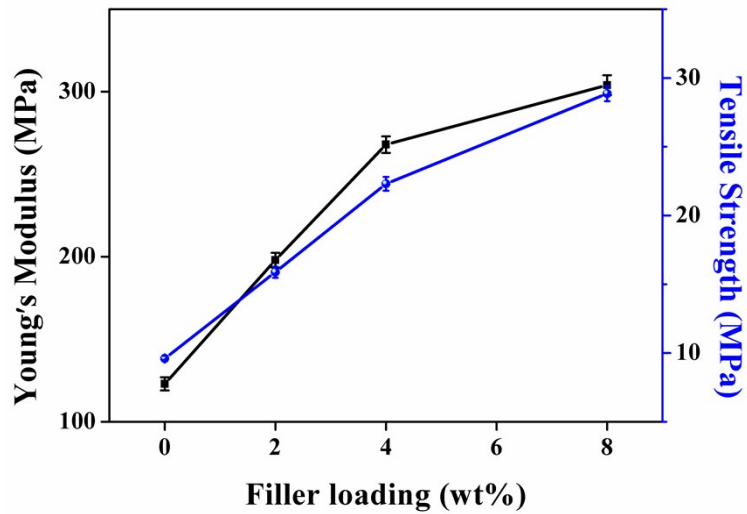


Fig. S8 Variation of Young's modulus and tensile strength of porous FPNC films with filler loadings (wt %).

S12: The reverse polarity test of porous FPNC films

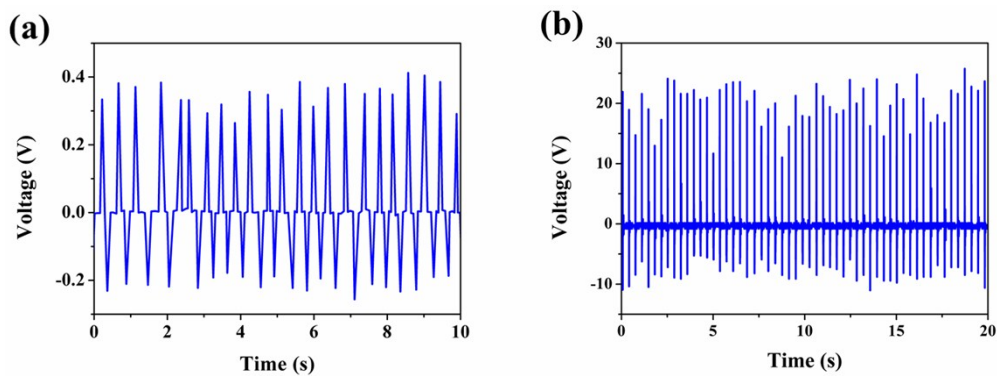


Fig. S9 (a) Current generated from FPNG based on pure PVDF film, (b) Output voltage (forward connection) from the FPNG (8) device which turns upside down

From Fig S9b, it can be seen that the nature of the voltage peaks remains the same along with the magnitude. This study indicates that the electrical signals from the device are generated from the material and not from the electrostatic interactions.

S13: The variation of output voltage of porous FPNC films with imparting pressure

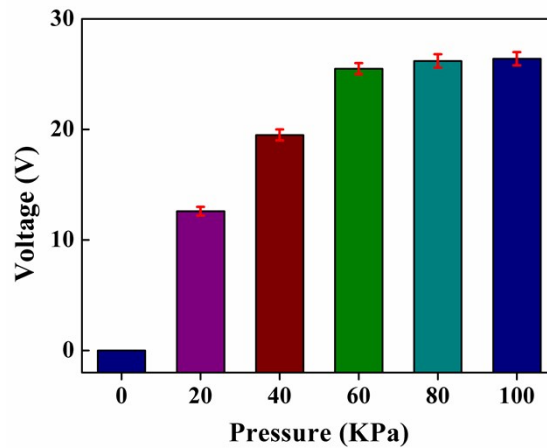


Fig. S10 The variation of the voltage generated from FPNG film with the applied pressure under fingers imparting.

S14: Power density calculation

$$\text{Power (P)} = V.I$$

$$= 26.2 \times 2.1 \mu\text{W} = 60.26 \mu\text{W}$$

$$\text{Power density} = \text{Power} / \text{area}$$

$$= 60.26/3.0 = 18.34 \mu\text{W}/\text{cm}^2$$

Here, $V=26.2$ V and $I=2.1$ μA are the maximum output voltage and current observed during finger imparting. The effective area of FPNC (8) film based FPNG (8) is 3.0 cm^2 .

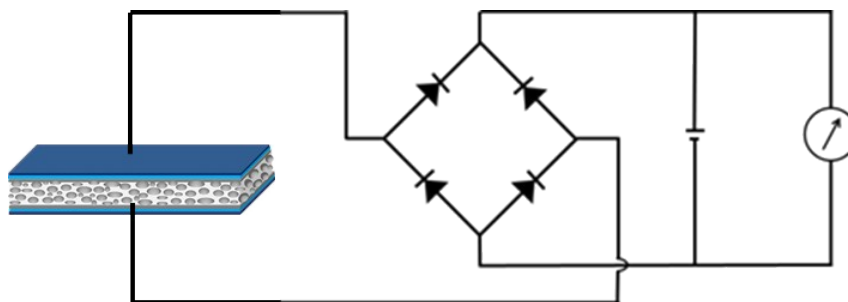


Fig. S11 Schematic showing the circuit diagram for rectification and storage of current generated from the device.

S15: Magnified portion of charging behavior of capacitors

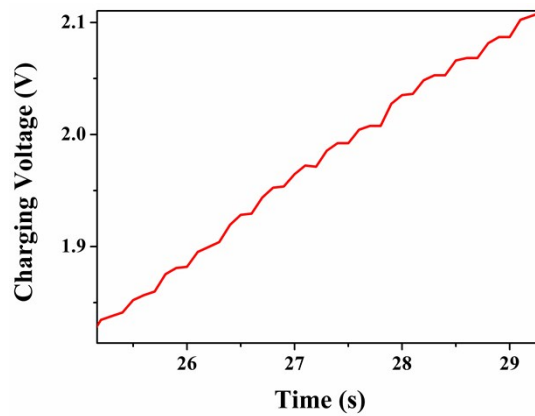


Fig. S12 Enlarged view of charging behaviour of capacitors ($1 \mu\text{F}$ capacitance) through FPNG (8) device

S16: Durability of FPNG device

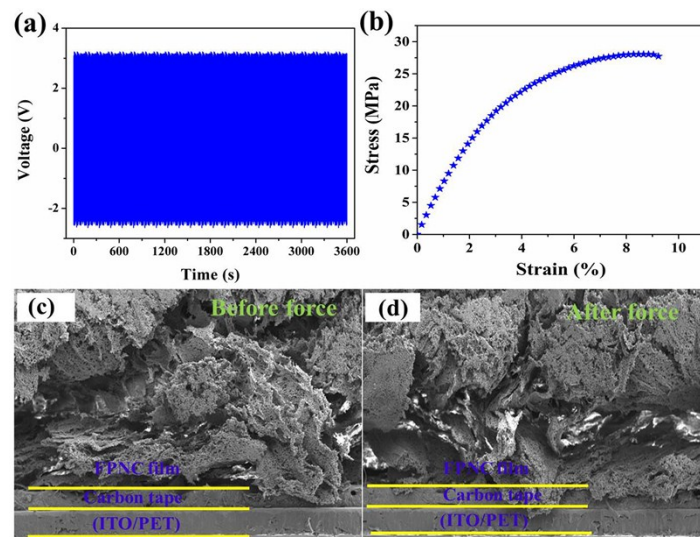


Fig. S13 (a) Stability and durability test of the FPNG under the sewing machine as a function of time over 3600 sec, (b) the stress-strain plot of the FPNC (8) which has been used for 4 weeks, (c) and (d) FE-SEM images (cross-sectional) of the FPNG (8) before force imparting and after force imparting on the device.

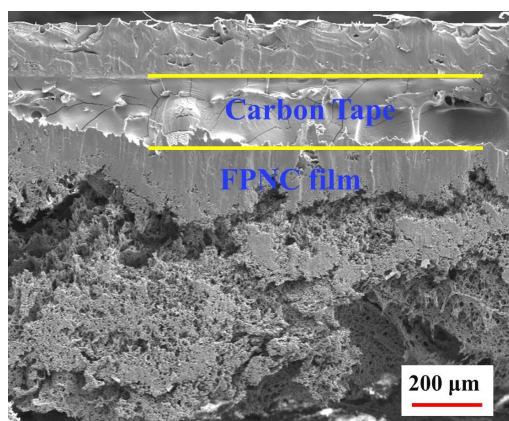


Fig. S14 Cross-sectional FE-SEM image of the FPNG (8) after force imparting on the device.

S17: The photocurrent response of PVPD, FPPD (2), FPPD (4) and FPD (8) devices:

We have measured the I-V performances of fabricated FPPD using pure PVDF, plain FAPbBr₃ NPs and PVDF/FAPbBr₃ composites under light illumination and dark condition; have shown in the Fig S15. Fig S15 (a) shows that photodetector based on pure PVDF (PVPD) does not response in presence of light illumination. But photodetectors (FPPD) based on FAPbBr₃/PVDF solution have generated the photocurrent in presence of light illumination, as shown in Fig. S15 (b) and (c). Under light illumination, the photocurrent (I_p) generated from the FPPD devices increases with an increase in the intensity of light (P) due to the increased number of charge carriers under the higher intensity of light¹³. This is due the presence of light absorbing formamidinium lead bromide NPs which generate the electron–hole under light illumination. In addition, photodetector based on only Formamidinium lead bromide (FPD) have generated better photocurrent under light illumination. The reason behinds this better performance of FPD is that the restriction in the charge flow by PVDF through breakage of the interconnected network which was formed by semiconducting FAPbBr₃ nanoparticles in FPPD.

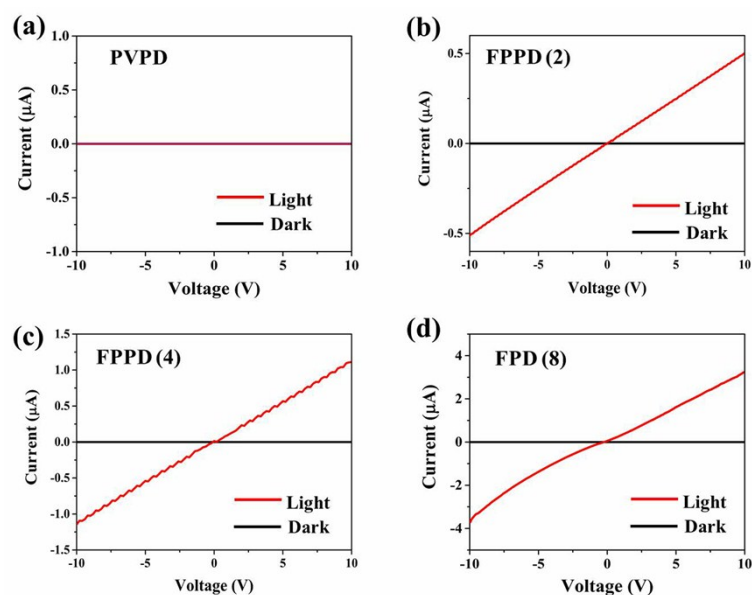


Fig. S15 Current-voltage characteristic curves of (a) PVPD, (b) FPPD (2), (c) FPPD (4) and FPD (8).

S18: Light detection ability of the pure PVDF film

Finally, to check the light detection ability of the pure PVDF film, a PVDF based piezoelectric energy nanogenerator (PPEN) has been fabricated for a self-powered light detector. The piezoelectric performances of the fabricated PPEN have been recorded under periodic stress in the dark and light illumination as a function of time, as shown in Fig. S16. Fig. S16 shows that the PPEN produces an output of ~ 5.2 V under dark but under light illumination (i.e., ON state), the amplitude of the piezoelectric response remains same ~ 16.1 V. As can be perceived, there appears almost no/zero deviation in the output voltage of the PVDF film under aforementioned conditions, whereas for FAPbBr₃/PVDF composites the decrease in output voltage solely due to the presence of FAPbBr₃ NPs, not due to the polymer chains.

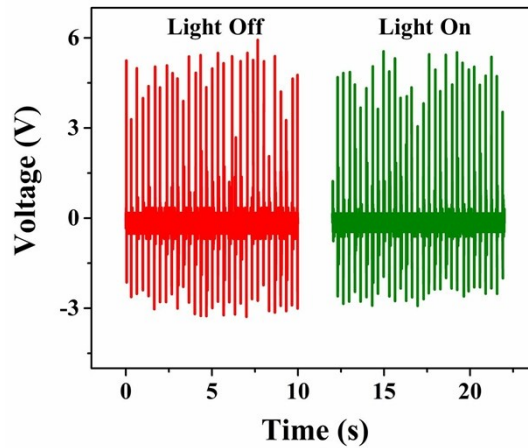


Fig. S16 Current-voltage characteristic curves of (a) PVPD, (b) FPPD (2), (c) FPPD (4) and FPD (8).

S19: Irradiance-dependent photocurrent

At a bias of 10 V, the illumination power-dependent photocurrent was plotted in Figure S17 with the irradiance intensity varying from 0.01mW.cm⁻² to 100 mW.cm⁻². The relationship between the photocurrent and the irradiance intensity can be fitted by the power law of

$$I_{ph} = a.P_0^x \dots\dots\dots(\text{ES9})$$

Where, I_{ph} represents photocurrent intensity, P represents irradiance power, a and x are the constant, exponential term respectively. From figure S17, the irradiance-dependent photocurrent curve was fitted to be I_{ph} ~ P^{0.03}.

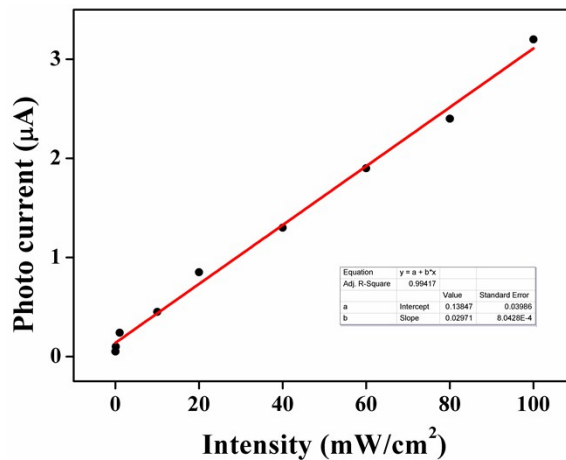


Fig. S17 Variation of photo current as a function of illumination intensity at a bias of 10 V

Supplementary Videos:

Supplementary Video1: The output performance of the FPNG under various conditions.

Supplementary Video2: Demonstration of the lighting of 21 red LEDs under finger imparting.

Supplementary Video3: Demonstration of the output performance of photoactive FPNG under light illumination.

References:

- 1 S. K. Karan, R. Bera, S. Paria, A. K. Das, S. Maiti, A. Maitra and B. B. Khatua, *Adv. Energy Mater.*, 2016, **6**.
- 2 S. K. Si, S. K. Karan, S. Paria, A. Maitra, A. K. Das, R. Bera, A. Bera, L. Halder and B. B. Khatua, *Mater. Chem. Phys.*, 2018, **213**, 525-537.
- 3 S. K. Karan, D. Mandal and B. B. Khatua, *Nanoscale*, 2015, **7**, 10655-10666.
- 4 M. S. S. Bafqi, R. Bagherzadeh and M. Latifi, *J. Polym. Res.*, 2015, **22**, 130.
- 5 C. V. Chanmal and J. P. Jog, *Int. J. Plast. Technol.*, 2011, **15**, 1.
- 6 R. Gonçalves, P. Martins, X. Moya, M. Ghidini, V. Sencadas, G. Botelho, N. D. Mathur and S. Lanceros-Méndez, *Nanoscale*, 2015, **7**, 8058-8061.
- 7 A. Sultana, M. M. Alam, P. Sadhukhan, U. K. Ghorai, S. Das, T. R. Middy and D. Mandal, *Nano Energy*, 2018, **49**, 380-392.
- 8 A. Sultana, P. Sadhukhan, M. M. Alam, S. Das, T. R. Middy and D. Mandal, *ACS Appl. Mater. Interfaces*, 2018, **10**, 4121-4130.
- 9 A. Sultana, S. K. Ghosh, M. M. Alam, P. Sadhukhan, K. Roy, M. Xie, C. R. Bowen, S. Sarkar, S. Das and T. R. Middy, *ACS Appl. Mater. Interfaces*, 2019, **11**, 27279-27287.
- 10 S. K. Karan, A. K. Das, R. Bera, S. Paria, A. Maitra, N. K. Shrivastava and B. B. Khatua, *RSC Adv.*, 2016, **6**, 37773-37783.

- 11 L. Huang, C. Lu, F. Wang and L. Wang, *RSC Adv.*, 2014, **4**, 45220-45229.
- 12 S. K. Karan, S. Maiti, A. K. Agrawal, A. K. Das, A. Maitra, S. Paria, A. Bera, R. Bera, L. Halder and A. K. Mishra, *Nano Energy*, 2019, **59**, 169-183.
- 13 S. Yang, S. Tongay, Y. Li, Q. Yue, J.-B. Xia, S.-S. Li, J. Li and S.-H. Wei, *Nanoscale*, 2014, **6**, 7226-7231.